

Electric-filed tuned anomalous valley Hall effect in A-type hexagonal antiferromagnetic monolayer

San-Dong Guo¹, Yu-Ling Tao¹, Zi-Yang Zhuo¹, Gangqiang Zhu² and Yee Sin Ang³

¹*School of Electronic Engineering, Xi'an University of Posts and Telecommunications, Xi'an 710121, China*

²*School of Physics and Electronic Information, Shaanxi Normal University, Xi'an 716000, Shaanxi, China and*

³*Science, Mathematics and Technology (SMT), Singapore University of Technology and Design, Singapore 487372*

The combination of antiferromagnetic (AFM) spintronics and anomalous valley Hall effect (AVHE) is of great significance for potential applications in valleytronics. Here, we propose a design principle for achieving AVHE in A-type hexagonal AFM monolayer. The design principle involves the introduction of layer-dependent electrostatic potential caused by out-of-plane external electric field, which can break the combined symmetry (PT symmetry) of spatial inversion (P) and time reversal (T), producing spin splitting. The spin order of spin splitting can be reversed by regulating the direction of electric field. Based on first-principles calculations, the design principle can be verified in AFM Cr_2CH_2 . The layer-locked hidden Berry curvature can give rise to layer-Hall effect, including valley layer-spin Hall effect and layer-locked AVHE. Our works provide an experimentally feasible way to realize AVHE in AFM monolayer.

Keywords: Valley, Antiferromagnetism, Electric field

Email:sandongyuwang@163.com

I. INTRODUCTION

Since the discovery and successful preparation of rich two-dimensional (2D) materials, valley has recently received extensive attention, which lays the foundation for processing information and performing logic operations with low power consumption and high speed, as valleytronics¹⁻⁴. Transition-metal dichalcogenide (TMD) monolayers are typical valleytronic materials with a pair of degenerate but inequivalent -K and K valleys in the reciprocal space⁵⁻¹⁰. The -K and K valleys exhibit opposite Berry curvature and selective absorption of chiral light. When including spin-orbit coupling (SOC), the valleys of -K and K points produce opposite spin splitting, characterized by spin-valley locking. However, these nonmagnetic TMD monolayers lack spontaneous valley polarization, which hinders the wide application of valleytronic devices. To achieve valley splitting, many methods have been applied, such as external magnetic field^{11,12}, proximity effect¹³⁻¹⁵, light excitation^{16,17}.

To realize intrinsic valley polarization, the ferrovalley semiconductor (FVS) has been proposed¹⁸, which appears in ferromagnetic (FM) materials with broken spatial inversion symmetry. Many 2D materials have been predicted to be FVS, such as 2H-VSe₂¹⁸, CrSi₂X₄ (X=N and P)¹⁹, VAgP₂Se₆²⁰, LaBr₂^{21,22}, VSi₂P₄²³, NbX₂ (X=S and Se)²⁴, Nb₃I₈²⁵, TiVI₆²⁶, FeClBr²⁷. Realizing valley polarization in antiferromagnetic (AFM) materials is more meaningful for valleytronic application, because AFM materials possess the high storage density, robustness against external magnetic field, as well as the ultrafast writing speed²⁸. Thus, it is of fundamental importance and high interest to achieve valley polarization in AFM materials, accompanied by anomalous valley Hall effect (AVHE).

However, both spontaneous valley polarization and AVHE are rarely reported in AFM monolayer. By stacking AFM monolayer MnPSe₃ or Cr₂CH₂ on ferroelectric

monolayer Sc₂CO₂, the AVHE has been achieved due to the introduction of nonuniform potentials to break the simultaneous time reversal and spatial inversion^{29,30}. Spin splitting and spontaneous valley polarization, accompanied by AVHE, have also been predicted in AFM Janus Mn₂P₂X₃Y₃ (X, Y=S, Se Te; X≠Y) monolayers by introducing an out-of-plane potential gradient⁴². Here, we propose a design principle for achieving AVHE in A-type hexagonal AFM monolayer by the introduction of layer-dependent electrostatic potential caused by out-of-plane external electric field. The spin order of spin splitting can be reversed, when the direction of electric field is flipped. By first-principles calculations, we translate design principle into Cr₂CH₂ monolayer and clarify the electric-filed-tuned valley physics.

II. WAYS TO ACHIEVE AVHE

The proposal for electric-filed tuned AVHE in AFM monolayer is schematically illustrated in **Figure 1**. We consider a hexagonal centrosymmetric monolayer with two-layer magnetic atoms with intralayer FM and interlayer AFM orderings (A-type AFM ordering), which possesses energy extrema of conduction or valance bands located at high symmetry -K and K points. The lattice of our proposed system has inversion symmetry, but the opposite spin vectors of the two sublattices break spatial inversion (P) symmetry and time reversal (T) symmetry, which produces spontaneous valley polarization (**Figure 1** (a)). However, the the spin degeneracy of -K and K valleys is maintained due to PT symmetry, which prohibits the AVHE in AFM monolayer.

There is zero berry curvature ($\Omega(k)$) everywhere in the momentum space due to PT symmetry. However, layer-locked hidden Berry curvature can appear, because each layer breaks the PT symmetry. Due to layer-spin locking, the Berry curvatures for the spin-up and spin-down

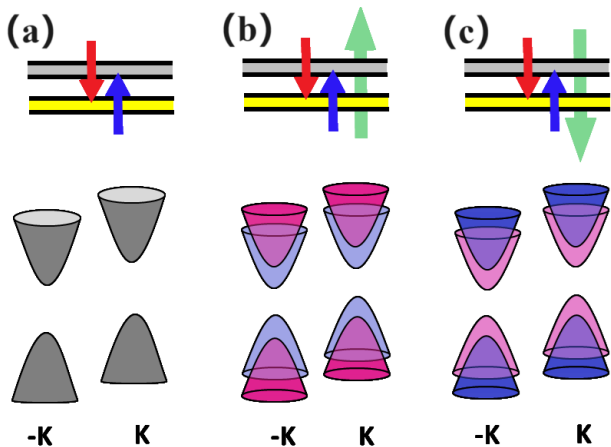


FIG. 1. (Color online) (a): a hexagonal A-type AFM monolayer with spin degeneracy but nonequivalent -K and K valleys; (b): by applying an out-of-plane electric field, the spin degeneracy is removed, and the -K and K valleys still are unequal; (c): when the direction of electric field is reversed, the order of spin splitting is also reversed. The spin-up and spin-down channels are depicted in blue and red.

channels are equal in magnitude and opposite in sign. The layer-locked hidden Berry curvature can give rise to layer-Hall effect.

Here, an out-of-plane electric field is applied to break the PT symmetry, which can remove spin degeneracy of -K and K valleys. The out-of-plane electric field can produce layer-dependent electrostatic potential $\propto eEd$ (e and d denote the electron charge and the layer distance.), which induces spin splitting effect. With breaking PT symmetry, the spin splitting at the -K and K valleys can be realized (Figure 1 (b)), resulting in the AVHE. Moreover, it is expected that the spin order at both the -K and K valleys can be reversed through manipulating the direction of out-of-plane electric field (Figure 1 (c)).

The H-functionalized MXene Cr_2C (Cr_2CH_2)⁴² can be used as a real material to verify our proposal. The Cr_2C is a half-metallic ferromagnet, which has been successfully synthesized in experiment⁴³. By surface functionalization with H in Cr_2C , a ferromagnetic-antiferromagnetic transition and a metal-insulator transition can be induced simultaneously⁴². In addition to this, Cr_2CH_2 possesses A-type AFM ordering with energy extrema of valance bands located at -K and K points, which meets the requirements of our proposal.

III. COMPUTATIONAL DETAIL

Within density functional theory (DFT)³², the spin-polarized first-principles calculations are carried out within the projector augmented-wave (PAW) method, as implemented in Vienna ab initio Simulation Package (VASP)^{33–35}. The generalized gradient approximation of Perdew-Burke-Ernzerhof (PBE-GGA)³⁶ as the exchange-

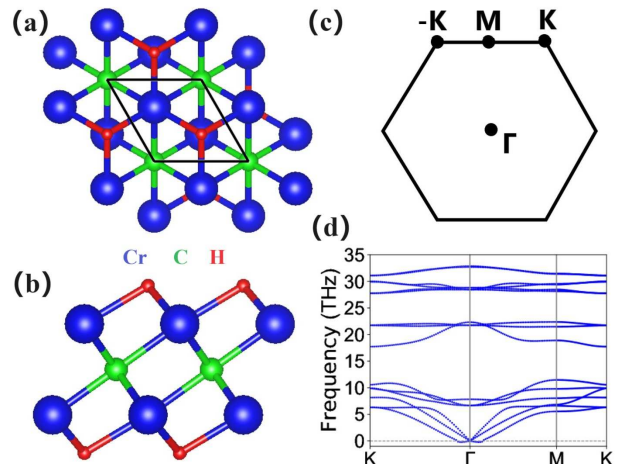


FIG. 2. (Color online) For monolayer Cr_2CH_2 , (a) and (b): the top and side views of crystal structures; (c): the first BZ with high symmetry points; (d): the phonon dispersion spectrum.

correlation functional is adopted. The kinetic energy cutoff of 500 eV, total energy convergence criterion of 10^{-8} eV, and force convergence criterion of $0.0001 \text{ eV} \cdot \text{\AA}^{-1}$ are set to obtain the accurate results. To account for the localized nature of Cr-3d orbitals, a Hubbard correction $U_{eff}=3.0 \text{ eV}$ ^{29,37} is used by the rotationally invariant approach proposed by Dudarev et al. The SOC is incorporated for investigation of valley splitting and magnetic anisotropy energy (MAE). The vacuum space of more than 20 \AA along z direction is introduced to avoid interactions between neighboring slabs. A $21 \times 21 \times 1$ Monkhorst-Pack k-point meshes are used to sample the Brillouin zone (BZ) for calculating electronic structures. Based on finite displacement method, the interatomic force constants (IFCs) are calculated by employing $5 \times 5 \times 1$ supercell with AFM ordering, and the phonon dispersion spectrum is obtained by the Phonopy code³⁸. The Berry curvatures are calculated directly from the calculated wave functions based on Fukui's method³⁹, as implemented in the VASPBERRY code^{40,41}.

IV. CRYSTAL AND ELECTRONIC STRUCTURES

It has been proved that Cr_2CH_2 monolayer possesses A-type AFM ordering with dynamical, mechanical, and thermal stabilities⁴². The crystal structures of Cr_2CH_2 along with the first BZ are shown in Figure 2 (a), (b) and (c), which crystallizes in the $P\bar{3}m1$ space group (No.164), hosting inversion symmetry. It consists of five atomic layers in the sequence of H-Cr-C-Cr-H, and the magnetic Cr atoms distribute in two layers. The optimized equilibrium lattice constants are $a=b=2.99 \text{ \AA}$ by GGA+ U method, which agrees well with previous result (2.95 \AA)⁴². Based on its energy band structures in FIG.S1 of elec-

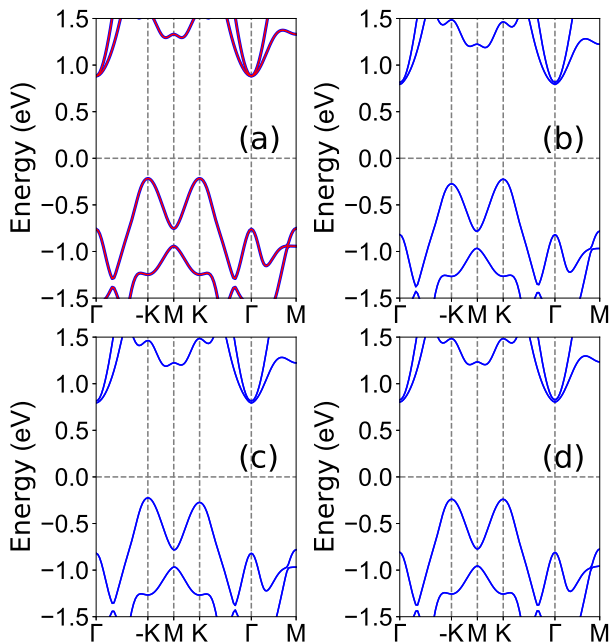


FIG. 3. (Color online) For Cr_2CH_2 , the energy band structures without SOC (a), and with SOC (b, c, d) for magnetization direction along the positive z , negative z , and positive x direction, respectively. In (a), the blue (red) lines represent the band structure in the spin-up (spin-down) direction.

tronic supplementary information (ESI) or in ref.⁴², the valence band maximum (VBM) of Cr_2CH_2 is at Γ point, not $-K$ or K point. To clearly clarify our proposal, the biaxial strain ($a/a_0=0.96$) is applied to change VBM of Cr_2CH_2 from Γ to $-K$ or K point. To determine magnetic ground state of Cr_2CH_2 , the FM and three AFM configurations (AFM1, AFM2 and AFM3) are constructed, as shown in FIG.S2 of ESI, and the AFM1 is called A-type AFM state. Calculated results show that the energy of AFM1 per unit cell is 281 meV, 50 meV and 399 meV lower than those of FM, AFM2 and AFM3 cases by GGA+ U , confirming that the strained Cr_2CH_2 still possesses AFM1 ground state. The calculated phonon spectrum of strained Cr_2CH_2 with no obvious imaginary frequencies is shown in Figure 2 (d), indicating its dynamic stability.

The energy band structures of Cr_2CH_2 by using both GGA and GGA+SOC are plotted in Figure 3. According to Figure 3 (a), no spin splitting can be observed due to the PT symmetry, and Cr_2CH_2 is an indirect band gap semiconductor. The energies of $-K$ and K valleys in the valence band are degenerate. Figure 3 (b) shows that the valley polarization can be induced by SOC, and the valley splitting is 49 meV. The energy of K valley is higher than one of $-K$ valley, and the valley polarization can be switched, when the magnetization direction is reversed (Figure 3 (c)). When the magnetization direction of Cr_2CH_2 is in-plane along x direction (Figure 3 (d)), no valley polarization can be observed. Therefore, the magnetic orientation is determined by MAE, which can

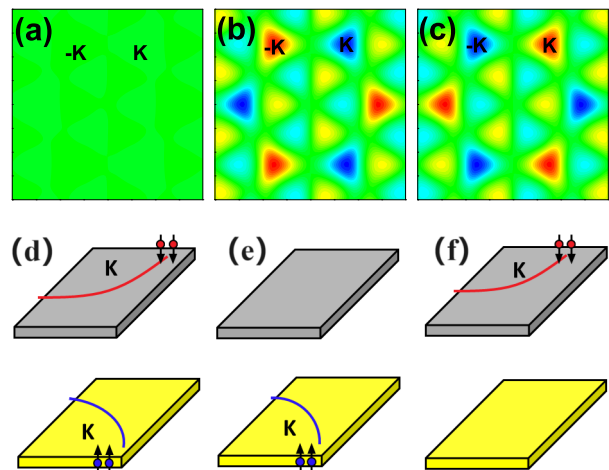


FIG. 4. (Color online) For Cr_2CH_2 , the distribution of Berry curvatures of total (a), spin-up (b) and spin-down (c). In the presence of a longitudinal in-plane electric field, an appropriate hole doping for three cases in Figure 1 produces valley layer-spin Hall effect (d) and layer-locked anomalous valley Hall effect (e and f). The upper and lower planes represent the top and bottom Cr layers.

be obtained by $E_{MAE} = E_{SOC}^{\parallel} - E_{SOC}^{\perp}$, where \parallel and \perp mean that spins lie in the plane and out-of-plane. The calculated MAE is $27\mu\text{eV}/\text{unit cell}$, indicating the out-of-plane easy magnetization axis of Cr_2CH_2 . This confirms the realization of our proposed design principles. The total magnetic moment of Cr_2CH_2 per unit cell is strictly $0.00 \mu_B$ with magnetic moment of bottom/top Cr atom being $3.09 \mu_B / -3.09 \mu_B$. When the SOC is included, the spin degeneracy is still maintained for both out-of-plane and in-plane magnetization directions.

For Cr_2CH_2 , the distribution of Berry curvatures of total, spin-up and spin-down are plotted in Figure 4. It is observed that total berry curvature everywhere in the momentum space is zero due to PT symmetry. The extremes of spin-resolved Berry curvatures locate at the $-K$ and K valleys, which have opposite signs for the same spin channel. For the same valley at different spin channel, the Berry curvatures are also opposite. When a longitudinal in-plane electric field is applied, the Bloch carriers will acquire an anomalous transverse velocity $v_{\perp} \sim E_{\parallel} \times \Omega(k)$ ⁴⁴. By shifting the Fermi level between the $-K$ and K valleys in the valence band, the spin-up and spin-down holes from K valley will accumulate along opposite sides of different layer under a longitudinal in-plane electric field, resulting in the valley layer-spin Hall effect (Figure 4 (d)), but the AVHE is absent.

V. ELECTRIC FIELD INDUCES SPIN SPLITTING

To induce spin splitting in Cr_2CH_2 , PT symmetry should be broken. Here, an out-of-plane electric field $+E$

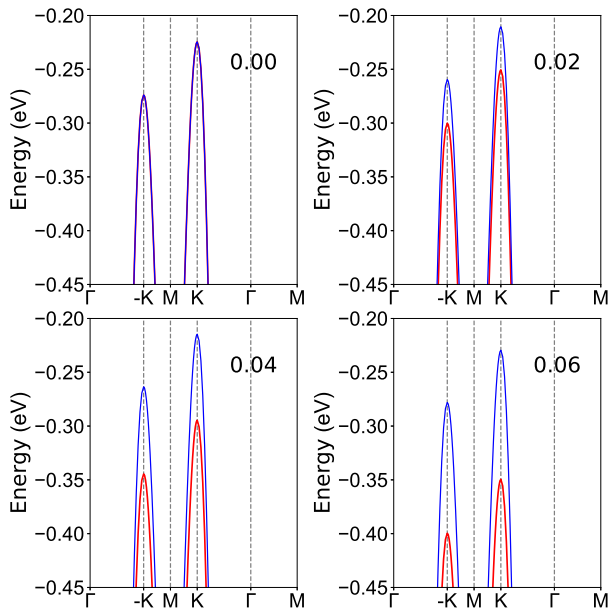


FIG. 5. (Color online) For Cr_2CH_2 , the spin-resolved energy band structures near the Fermi level for the valence band with SOC at representative E .

(0.00-0.10 V/Å) is applied, which can break PT symmetry, and lift spin degeneracy of valleys. The $-E$ generates exactly the same results except spin orders since two Cr layers are related by a glide mirror G_z symmetry, but have opposite magnetic moments. Firstly, the magnetic ground state under out-of-plane electric field is determined by the energy difference between FM/AFM2/AFM3 and AFM1 configurations. Within considered E range, based on FIG.S3 of ESI, the AFM1 ordering is always ground state. The MAE vs E is plotted in FIG.S4, and the positive MAE confirms that the easy axis of Cr_2CH_2 is out-of-plane direction within considered E range. These ensure that our design principles can be realized in Cr_2CH_2 .

The energy band structures of Cr_2CH_2 at representative E by using GGA+SOC are plotted in FIG.S5 of ESI, and the enlarged figures of spin-resolved energy band structures near the Fermi level for the valence band are shown in Figure 5. For valence band, the valley splitting and spin splitting at -K and K valleys as a function of E are plotted in Figure 6. The spontaneous valley polarization of about 49 meV is maintained within considered E range. When electric field is applied, it is clearly seen that there is spin splitting, which is due to layer-dependent electrostatic potential caused by out-of-plane electric field. Spin splitting and electric field strength show a linear relationship. In fact, the spin splitting can be approximately calculated by eEd . Taking $E=0.02\text{V}/\text{Å}$ as an example, the d of Cr_2CH_2 is 2.37 Å, and the estimated spin splitting is approximately 47 meV, which is close to the first-principle result 41 meV. The coexistence of spin splitting and valley polarization is essential for the realization of AVHE. When the electric

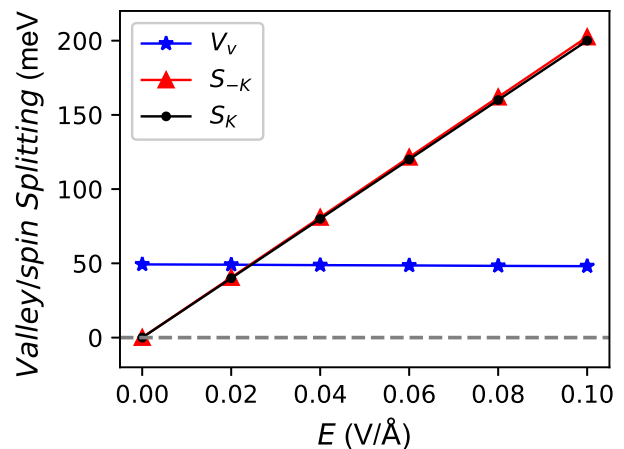


FIG. 6. (Color online) For Cr_2CH_2 , the valley splitting (V_v) and spin splitting (S_{-K} and S_K at -K and K valleys) for valence band as a function of E .

field changes from $+E$ to $-E$, the layer-dependent electrostatic potential is also reversed. The sizes of spin splitting and valley splitting remain unchanged, but the spin order of spin splitting reversed (FIG.S6 of ESI), which is consistent with our proposed design principle.

For Cr_2CH_2 at $E=0.02\text{V}/\text{Å}$, the distribution of Berry curvatures of spin-up and spin-down are shown in FIG.S7. It is clearly seen that the Berry curvatures are opposite for the same valley at different spin channel and different valley at the same spin channel. By shifting the Fermi level between the -K and K valleys in the valence band, only the spin-up holes from the K valley move to the bottom boundary of the sample under an in-plane electric field (Figure 4 (e)), producing layer-locked AVHE. Conversely, by reversing the electric field direction, the spin-down holes from the K valley will move to the top opposite side of the sample by proper hole doping (Figure 4 (f)). This accumulation of spin-polarized holes produces a net charge/spin current, and Figure 4 (e) and Figure 4 (f) generate opposite voltage.

VI. CONCLUSION

In summary, we present a model to induce AVHE in A-type hexagonal AFM monolayer by applying electric field. The validity of our proposal is confirmed by an extensive study of Cr_2CH_2 within the first-principles calculations. The spontaneous valley polarization can occur in Cr_2CH_2 , but the spin splitting of -K and K valleys is absent. The introduction of an out-of-plane electric field results in spin splitting due to layer-dependent electrostatic potential. The layer-locked hidden Berry curvature produces layer-locked AVHE. Our work enriches the AVHE in AFM monolayers, and provides great potential for developing energy-efficient and ultrafast valleytronic devices.

ACKNOWLEDGMENTS

This work is supported by Natural Science Basis Research Plan in Shaanxi Province of China (2021JM-456).

We are grateful to Shanxi Supercomputing Center of China, and the calculations were performed on TianHe-2.

-
- ¹ J. R. Schaibley, H. Yu, G. Clark, P. Rivera, J. S. Ross, K. L. Seyler, W. Yao and X. Xu, *Nat. Rev. Mater.* **1**, 16055 (2016).
 - ² G. Pacchioni, *Nat. Rev. Mater.* **5**, 480 (2020).
 - ³ S. A. Vitale, D. Nezhich, J. O. Varghese, P. Kim, N. Gedik, P. Jarillo-Herrero, D. Xiao and M. Rothschild, *Small* **14**, 1801483 (2018).
 - ⁴ D. Xiao, M. C. Chang and Q. Niu, *Rev. Mod. Phys.* **82**, 1959 (2010).
 - ⁵ A. Srivastava, M. Sidler, A. V. Allain, D. S. Lembke, A. Kis and A. Imamoglu, *Nat. Phys.* **11**, 141 (2015).
 - ⁶ K. F. Mak, K. He, J. Shan and T. F. Heinz, *Nat. Nanotechnol.* **7**, 494 (2012).
 - ⁷ H. Zeng, J. Dai, W. Yao, D. Xiao, and X. Cui, *Nat. Nanotechnol.* **7**, 490 (2012).
 - ⁸ M. Zeng, Y. Xiao, J. Liu, K. Yang and L. Fu, *Chem. Rev.* **118**, 6236 (2018).
 - ⁹ C. Zhao, T. Norden, P. Zhang, P. Zhao, Y. Cheng, F. Sun, J. P. Parry, P. Taheri, J. Wang, Y. Yang, T. Scrace, K. Kang, S. Yang, G. Miao, R. Sabirianov, G. Kioseoglou, W. Huang, A. Petrou and H. Zeng, *Nat. Nanotechnol.* **12**, 757 (2017).
 - ¹⁰ D. MacNeill, C. Heikes, K. F. Mak, Z. Anderson, A. Kormányos, V. Zólyomi, J. Park and D. C. Ralph, *Phys. Rev. Lett.* **114**, 037401 (2015).
 - ¹¹ X. X. Zhang, Y. Lai, E. Dohner, S. Moon, T. Taniguchi, K. Watanabe, D. Smirnov and T. F. Heinz, *Phys. Rev. Lett.* **122**, 127401 (2019).
 - ¹² D. MacNeill, C. Heikes, K. F. Mak, Z. Anderson, A. Kormányos, V. Zólyomi, J. Park and D. C. Ralph, *Phys. Rev. Lett.* **114**, 037401 (2015).
 - ¹³ L. Xu, M. Yang, L. Shen, J. Zhou, T. Zhu and Y. P. Feng, *Phys. Rev. B* **97**, 041405 (2018).
 - ¹⁴ C. Zhao, T. Norden, P. Zhang, P. Zhao, Y. Cheng, F. Sun, J. P. Parry, P. Taheri, J. Wang, Y. Yang, T. Scrace, K. Kang, S. Yang, G. Miao, R. Sabirianov, G. Kioseoglou, W. Huang, A. Petrou and H. Zeng, *Nat. Nanotechnol.* **12**, 757 (2017).
 - ¹⁵ W. Zhou, Z. Yang, A. Li, M. Long and F. Ouyang, *Phys. Rev. B* **101**, 045113 (2020).
 - ¹⁶ T. Cao, G. Wang, W. Han, H. Ye, C. Zhu, J. Shi, Q. Niu, P. Tan, E. Wang, B. Liu and J. Feng, *Nat. Commun.* **3**, 887 (2012).
 - ¹⁷ L. Xie and X. Cui, *Proc. Natl. Acad. Sci. USA* **113**, 3746 (2016).
 - ¹⁸ W. Y. Tong, S. J. Gong, X. Wan and C. G. Duan, *Nat. Commun.* **7**, 13612 (2016).
 - ¹⁹ Y. B. Liu, T. Zhang, K. Y. Dou, W. H. Du, R. Peng, Y. Dai, B. B. Huang, and Y. D. Ma, *J. Phys. Chem. Lett.* **12**, 8341 (2021).
 - ²⁰ Z. Song, X. Sun, J. Zheng, F. Pan, Y. Hou, M.-H. Yung, J. Yang, and J. Lu, *Nanoscale* **10**, 13986 (2018).
 - ²¹ J. Zhou, Y. P. Feng, and L. Shen, *Phys. Rev. B* **102**, 180407(R) (2020).
 - ²² P. Zhao, Y. Ma, C. Lei, H. Wang, B. Huang, and Y. Dai, *Appl. Phys. Lett.* **115**, 261605 (2019).
 - ²³ X. Y. Feng, X. L. Xu, Z. L. He, R. Peng, Y. Dai, B. B. Huang and Y. D. Ma, *Phys. Rev. B* **104**, 075421 (2021)
 - ²⁴ Y. Zang, Y. Ma, R. Peng, H. Wang, B. Huang, and Y. Dai, *Nano Res.* **14**, 834 (2021).
 - ²⁵ R. Peng, Y. Ma, X. Xu, Z. He, B. Huang, and Y. Dai, *Phys. Rev. B* **102**, 035412 (2020).
 - ²⁶ W. Du, Y. Ma, R. Peng, H. Wang, B. Huang, and Y. Dai, *J. Mater. Chem. C* **8**, 13220 (2020).
 - ²⁷ R. Li, J. W. Jiang, W. B. Mi and H. L. Bai, *Nanoscale* **13**, 14807 (2021).
 - ²⁸ T. Jungwirth, J. Sinova, A. Manchon, X. Marti, J. Wunderlich, and C. Felser, *Nat. Phys.* **14**, 200 (2018).
 - ²⁹ T. Zhao, S. Xing, J. Zhou, N. Miao and Z. Sun, *Journal of Materiomics* (2023), doi: <https://doi.org/10.1016/j.jmat.2023.10.008>.
 - ³⁰ W. Du, R. Peng, Z. He, Y. Dai, B. Huang, and Y. Ma, *npj 2D Mater. Appl.* **6**, 11 (2022).
 - ³¹ Y. Xu, H. Liu, Y. Dai, B. Huang and W. Wei, *Appl. Phys. Lett.* **122**, 242404 (2023).
 - ³² P. Hohenberg and W. Kohn, *Phys. Rev.* **136**, B864 (1964); W. Kohn and L. J. Sham, *Phys. Rev.* **140**, A1133 (1965).
 - ³³ G. Kresse, *J. Non-Cryst. Solids* **193**, 222 (1995).
 - ³⁴ G. Kresse and J. Furthmüller, *Comput. Mater. Sci.* **6**, 15 (1996).
 - ³⁵ G. Kresse and D. Joubert, *Phys. Rev. B* **59**, 1758 (1999).
 - ³⁶ J. P. Perdew, K. Burke and M. Ernzerhof, *Phys. Rev. Lett.* **77**, 3865 (1996).
 - ³⁷ J. He, G. Ding, C. Zhong, S. Li, D. Li and G. Zhang, *Nanoscale*, **11**, 356 (2018).
 - ³⁸ A. Togo, F. Oba and I. Tanaka, *Phys. Rev. B* **78**, 134106 (2008).
 - ³⁹ T. Fukui, Y. Hatsugai and H. Suzuki, *J. Phys. Soc. Japan.* **74**, 1674 (2005).
 - ⁴⁰ H. J. Kim, <https://github.com/Infant83/VASPBERRY>, (2018).
 - ⁴¹ H. J. Kim, C. Li, J. Feng, J.-H. Cho, and Z. Zhang, *Phys. Rev. B* **93**, 041404(R) (2016).
 - ⁴² C. Si, J. Zhou and Z. Sun, *ACS Appl. Mater. Interfaces* **7**, 17510 (2015).
 - ⁴³ B. Soundiraraju, R. Raghavan and B.K. George, *ACS Appl. Nano Mater.* **3**, 11007 (2020).
 - ⁴⁴ D. Xiao, M. C. Chang and Q. Niu, *Rev. Mod. Phys.* **82**, 1959 (2010).